

Magnetic-field Induced Interconversion of Cooper Pairs and Density Wave States within Cuprate Composite Order

M. H. Hamidian^{1†}, S. D. Edkins^{1,2†}, K. Fujita^{1,2,3}, A. Kostin¹, A. P. Mackenzie^{2,5}, H. Eisaki⁶, S. Uchida⁴, M. J. Lawler^{1,7}, E.-A. Kim¹, S. Sachdev⁸ and J. C. Davis^{1,2,3}

1. *LASSP, Department of Physics, Cornell University, Ithaca, NY 14853, USA.*
2. *School of Physics and Astron., University of St. Andrews, Fife KY16 9SS, Scotland.*
3. *CMPMS Department, Brookhaven National Lab., Upton NY, USA.*
4. *Department of Physics, University of Tokyo, Bunkyo-ku, Tokyo 113-0033, Japan.*
5. *Max-Planck Institute for Chemical Physics of Solids, D-01187 Dresden, Germany.*
6. *Inst. of Advanced Industrial Science and Tech., Tsukuba, Ibaraki 305-8568, Japan.*
7. *Dept. of Physics and Astronomy, Binghamton University, Binghamton, NY 13902, USA.*
8. *Department of Physics, Harvard University, Cambridge, MA 02138, USA.*

[†] These authors contributed equally to this project.

Recent studies establish that the cuprate pseudogap phase is susceptible at low temperatures to forming not only a *d*-symmetry superconducting (SC) state, but also a *d*-symmetry form factor (dFF) density wave (DW) state. The concurrent emergence of such distinct and unusual states from the pseudogap motivates theories that they are “intertwined” i.e. derived from a quantum composite of dissimilar broken-symmetry orders. Some composite order theories predict that the balance between the different components can be altered, for example at superconducting vortex cores. Here, we introduce sublattice phase-resolved electronic structure imaging as a function of magnetic field and find robust dFF DW states induced at each vortex. They are predominantly unidirectional and co-oriented (nematic), exhibiting strong spatial-phase coherence. At each vortex, we also detect the field-induced conversion of the SC to DW components, and demonstrate that this occurs at precisely the eight momentum-space locations predicted in many composite order theories. These data provide direct microscopic evidence for the existence of composite order in the cuprates, and new indications of how the DW state becomes long-range ordered in high magnetic fields.

2 The cuprate pseudogap phase (PG) emerges from an antiferromagnetic insulator state (Fig. 1A) when electrons are removed from the oxygen orbitals of the CuO_2 plane (1-3). Although the precise identity of the PG remains ambiguous, its low temperature limit transforms into superconductivity having d -symmetry (1,2). Recent studies establish that the PG is also susceptible to generating an exotic density wave state, with axial wavevector $\vec{Q} = (Q, 0); (0, Q)$ and a predominantly d -symmetry form factor (4-12). This unconventional DW has now been identified in $\text{YBa}_2\text{Cu}_3\text{O}_{7-x}$, $\text{Bi}_2\text{Sr}_2\text{CaCu}_2\text{O}_{8+x}$, $\text{Bi}_2\text{Sr}_2\text{CuO}_{6+x}$ and $\text{Ca}_{2-x}\text{Na}_x\text{CuO}_2\text{Cl}_2$ (13-17). The parallel emergence of such unusual and dissimilar states from the PG at approximately the same temperature and carrier-density has motivated recent theories that they are “intertwined” (18,19), i.e. derived from an overarching composite of multiple distinct broken-symmetry orders (19-29). An immediate challenge for cuprate studies is therefore to search for direct microscopic evidence for such composite order.

3 Advances have also occurred in understanding the electronic structure of the PG at very high magnetic fields where the superconductivity is suppressed (30). Here, the observed quantum oscillations (QO) are used to adduce a new momentum-space (\vec{k} -space) structure consisting of small electron-pockets (30). One important and unusual effect of magnetic fields is to enhance the intensity of the cuprate DW dramatically, but only when superconductivity is present (31-36). Moreover, evidence is now accumulating that, as the field is increased, a transition occurs to a new long-range ordered DW state (34,37,38). The global broken symmetries of this unknown high-field state would then be the proximate cause of a Fermi surface reconstruction (30, 39) that produces the exotic QO phenomenology (30). Observation of field-induced DW amplification only in the SC state has frequently motivated hypotheses that that interplay of DW and SC states occurs at quantized vortex cores, where superconductivity is suppressed. However, it has not yet been demonstrated directly that the field-induced DW effects detected by bulk probes (31-38) are actually occurring at the vortex cores. And if they are, precisely which symmetries

are broken at these cores, and microscopically how the field-induced interplay between SC and DW states occurs therein, are all unknown.

4 Composite order (CO) theories for the cuprates posit that instabilities of the PG to different broken-symmetry (ordered) states are occurring because these states all derive from an overarching state made up of distinct component orders that are energetically degenerate, or at least appear so at high temperatures (20-29). The most often studied possibilities for the constituents of such a composite state are superconductivity (SC), a charge density wave (CDW) with wavevector \vec{Q} , and a pair density wave (PDW) or modulated superconducting state with wavevector \vec{Q}' . Order parameters for each can be written:

$$SC = \langle \psi_{k,\sigma}^\dagger \psi_{-k,-\sigma}^\dagger \rangle \quad (1a)$$

$$CDW = \langle \psi_{k,\sigma}^\dagger \psi_{k+Q,\sigma} \rangle \quad (1b)$$

$$PDW = \langle \psi_{k,\sigma}^\dagger \psi_{-k+Q',-\sigma}^\dagger \rangle \quad (1c)$$

where $\psi_{k,\sigma}^\dagger$ and $\psi_{k,\sigma}$ represent creation and annihilation of $|k(E), \sigma\rangle$ eigenstates with momentum $\vec{p} = \hbar\vec{k}$ and spin $\vec{S} = \hbar\vec{\sigma}$; a variety of possible \vec{Q} and DW form factors have been considered for these orders. A hypothetical composite of two orders in Eqn. 1 would then have contributions with different order-parameter amplitudes (22,23,25,26,28) that are concentrated at a specific set of $|\vec{k}(E)\rangle$ eigenstates where the mixing of these orders occurs predominantly (22,23,25,26). The \vec{k} -space locations most often predicted for these effects to occur are indicated schematically by the black circles in Fig. 1B.

5 Several CO theories then predict that, if the PG order is a composite from which the DW and SC states emerge, this might be revealed by altering the balance between them at vortex cores (26-29). In principle this would: (i) alter the relative amplitude of SC and DW components and, (ii) occur primarily at specific $|\vec{k}(E)\rangle$ eigenstates where interactions of SC

and DW components are predominant (Fig. 1B). These \vec{k} -space locations are special because either interactions of the $|\vec{k}(E)\rangle$ eigenstates with antiferromagnetic spin fluctuations (20-23,25,27-29), or with preexisting $\vec{Q} \cong (1/4,0)(0,1/4)2\pi/a$ density waves (19), are concentrated there. For direct experimental exploration of these ideas, studies slightly below optimal doping would seem best because it is here that the different known states (PG, DW, SC) are approximately equal in strength and thus most delicately balanced (vertical arrow Fig. 1A). The experimental challenge would then be to find the signature of a field-induced interconversion of SC to DW states for some particular set of $|\vec{k}(E)\rangle$ eigenstates, with these effects only occurring within the nanoscale regions surrounding each vortex core. One way to achieve this is to use spectroscopic imaging scanning tunneling microscopy (Ref.40,41), a technique that allows simultaneous access to real space (\vec{r} -space) electronic structure directly, and to \vec{k} -space electronic structure using quasiparticle interference imaging (QPI) (40,41).

7 The unconventional DW state of cuprates has only been detected within the pseudogap regime (17,40,42,43). Moreover, we now know that it exhibits a predominantly d -symmetry form factor in the compounds $\text{Bi}_2\text{Sr}_2\text{CaCu}_2\text{O}_{8+x}$, $\text{Bi}_2\text{Sr}_2\text{Cu}_1\text{O}_{6+x}$, $\text{Na}_x\text{Ca}_{2-x}\text{ClCuO}_2$, and $\text{YBa}_2\text{Cu}_3\text{O}_{6+x}$ (Refs.13-17). Specifically, this means that the DW modulations at the two oxygen sites (O_x, O_y) within every CuO_2 unit cell are out of phase by π (SI Section 1). Thus, the amplitude of whatever electronic/lattice degree-of-freedom is being modulated in the DW can be written as $A(\vec{r}) = D(\vec{r})\text{Cos}(\vec{Q} \cdot \vec{r} + \phi(\vec{r}))$, where $D(\vec{r})$ is the d -symmetry form factor having opposite sign on the O_x and O_y sublattices, \vec{Q} is the characteristic wavevector of the DW, and $\phi(\vec{r})$ is a potentially disordered spatial phase (13,17). Such a dFF DW can be visualized directly with scanning tunneling microscopy by measuring the differential tunneling conductance $\frac{dI}{dV}(\vec{r}, E = eV) \equiv g(\vec{r}, E)$ and the tunneling current $I(\vec{r}, E)$ at locations \vec{r} and bias voltage V . The images $Z(\vec{r}, |E|) \equiv g(\vec{r}, +V)/g(\vec{r}, -V)$ or $R(\vec{r}, |E|) \equiv |I(\vec{r}, +V)/I(\vec{r}, -V)|$ then allow energy magnitudes, wavelengths

and spatial phases to be measured without the profound systematic errors from the “setup effect” (40). The spatial phase throughout each $Z(\vec{r}, |E|)$ is first defined precisely (40), and then two new sublattice images $O_x(\vec{r}), O_y(\vec{r})$ containing only the measured signal at the x/y-axis oxygen sites, are derived (13,17). The Fourier transforms of $O_x(\vec{r})$ and $O_y(\vec{r})$, $\tilde{O}_x(\vec{q}) = \text{Re}\tilde{O}_x(\vec{q}) + i\text{Im}\tilde{O}_x(\vec{q})$ and $\tilde{O}_y(\vec{q}) = \text{Re}\tilde{O}_y(\vec{q}) + i\text{Im}\tilde{O}_y(\vec{q})$, then yield

$$\tilde{D}^Z(\vec{q}, |E|) = \tilde{O}_x(\vec{q}, V) - \tilde{O}_y(\vec{q}, V) \quad (2)$$

where the superscript identifies the original image type being analyzed. Detecting a local maximum in $\tilde{D}^Z(\vec{q}, |E|)$ at any finite \vec{q} inside the first Brillouin zone is then the distinctive signature of *d*-symmetry form factor modulations (13,17). The equivalent role for the *s*'-symmetry form factor modulations that are in-phase between the O_x and O_y sublattices is played by

$$\tilde{S}'^Z(\vec{q}, |E|) = \tilde{O}_x(\vec{q}, V) + \tilde{O}_y(\vec{q}, V) \quad (3)$$

Figure 1C shows a typical measured $Z(\vec{r}, |E|)$ image of the dFF DW state of underdoped $\text{Bi}_2\text{Sr}_2\text{CaCu}_2\text{O}_{8-x}$ at $p \sim 12\%$ and $|E| = 100\text{meV}$, while Fig. 1D shows the $|\tilde{D}^Z(\vec{q}, 100\text{meV})|$ derived from it using Eqn. 2. The signature of the dFF DW state is highlighted by dashed red circles surrounding its two characteristic wavevectors $\vec{Q} = (Q, 0); (0, Q)$. Figure 1E shows one wavelength of a typical high-resolution \vec{r} -space image of such a cuprate dFF DW modulation (13,17) along \vec{Q}_y . At zero field, this type of sublattice phase-resolved imaging has revealed that the underdoped cuprate DW exhibits a predominantly *d*-symmetry form factor (13,17); that it maintains this form factor symmetry throughout the whole pseudogap region of the phase diagram (17); that its \vec{r} -space arrangement consists of nanoscale regions each containing a unidirectional dFF DW (17); and that the characteristic energy of the dFF DW electronic structure modulations is actually the pseudogap energy (17).

8 Here, to visualize if and how a composite order of the SC and DW components is altered by magnetic fields (26-29), we measure the field dependent $Z(\vec{r}, E, B)$ at 2K for slightly underdoped samples ($T_c \sim 88\text{K}$; $p \sim 17\%$) and for $0 < |E| < 80\text{meV}$ in magnetic fields up to $B = 8.5\text{T}$. We use measurements with more than 25 pixels within each CuO_2 unit cell while using a sufficiently large FOV (typically $65\text{nm} \times 65\text{nm}$) to achieve high resolution in spatial phase definition; we then image $Z(\vec{r}, |E|, B)$ in precisely the same FOV at $B = 0$ and $B = 8.5\text{T}$. The spatial phase for each of the sublattice images $O_x(\vec{r}), O_y(\vec{r})$ is determined and the $Z(\vec{r}, |E|, 0)$ and $Z(\vec{r}, |E|, B)$ images are registered to each other in every CuO_2 unit cell with $\sim 10\text{ pm}$ precision. Finally the two $Z(\vec{r}, |E|, B)$ sets are subtracted to yield the field-induced effects on electronic structure $\delta Z(\vec{r}, |E|, B)$ (SI Section 2). The location of every vortex core is identified by using two well-known phenomena: (i) suppression of the superconducting coherence peaks and, (ii) appearance of periodic Bogoliubov quasiparticle modulations at $|E| < 0.25\Delta_{\text{SC}}$ (44,45). To allow comparison with earlier works, Fig. 2A shows $\delta g(\vec{r}, 10\text{meV}) = g(\vec{r}, 10\text{meV}, 8.5\text{T}) - g(\vec{r}, 10\text{meV}, 0\text{T})$, the field-induced change in conductance at $|E| = 10\text{meV}$. This illustrates the excellent agreement with previous studies of low energy quasiparticle modulations at $\text{Bi}_2\text{Sr}_2\text{CaCu}_2\text{O}_{8-x}$ vortex cores (44,45).

9 The more physically accurate $\delta Z(\vec{r}, |E|) = Z(\vec{r}, |E|, 8.5\text{T}) - Z(\vec{r}, |E|, 0\text{T})$ is used in throughout subsequent analysis. In the same FOV we use our sublattice phase-resolved $\delta Z(\vec{r}, |E|)$ data to determine $\tilde{D}^{\delta Z}(\vec{q}, |E|)$ and $\tilde{S}'^{\delta Z}(\vec{q}, |E|)$ as specified by Eqn. 1,2. Figure 2B,D show $\tilde{D}^{\delta Z}(\vec{q}, |E|)$ at $|E| = 10\text{meV}$ and $|E| = 30\text{meV}$ respectively, with Fig. 2D calculated from $\delta Z(\vec{q}, 30\text{meV})$ as shown in Fig. 2C. The primary and most significant differences between 2B and 2D are the clear signatures of d -symmetry form factor modulations at \vec{Q}_x, \vec{Q}_y for $|E| = 30\text{meV}$ in the latter, that are absent in the former. In general, our sublattice phase-resolved imaging reveals that, at higher energy the field-induced $\delta Z(\vec{r}, |E|)$ exhibits primarily dFF-DW states. Moreover, as seen directly from unprocessed data in Fig. 2C,

these phenomena occur at the sites of vortex cores. Figure 2E shows a close-up image of one of these vortex core sites in which the \vec{r} -space signature of a dFF DW regions is evident; the grey inset compares a canonical dFF DW element from strongly underdoped sample. Finally, we visualize directly where field-induced dFF DW intensity occurs throughout \vec{r} -space; Figure 2F shows an image of the measured magnitude of $|\tilde{D}^{\delta Z}(\vec{r}, 30meV)|$ i.e. the regions of space supporting a strong field-induced dFF DW (SI Section 3). By comparison with Fig. 2A one sees that they occur at and only at the sites of quantized vortex cores.

10 Next, we consider the issues of which spatial symmetries are broken at the cuprate vortex core. Figure 3A shows the $|\tilde{D}^{\delta Z}(\vec{q}, 30meV)|$ whose two peaks at \vec{Q}_x and \vec{Q}_y derive almost completely from the region of vortex cores (Fig. 2F). We consider their relative magnitude in Fig. 3A by plotting $|\tilde{D}^{\delta Z}(\vec{q}, 30meV)|$ along the x-axis (orange) and y-axis (green). The enhancement of dFF DW averaged over all cores is ~ 3 times more intense in y-direction, meaning that the dFF DW modulations are occurring predominantly in this direction. To visualize the predominantly \vec{Q}_y modulations in \vec{r} -space, we plot in Fig. 3B the measured structure of dFF-DW at \vec{Q}_y in the regions of all stable vortex cores from Fig. 2C (SI Section 4). Overlaid for reference are lines of constant phase (grey) for a modulation at wavelength $\lambda_y = 2\pi/Q_y$. The nematic (19,26) co-orientation of the field-induced dFF DW states at the vortex cores is clear from the strong maximum at $\vec{Q}_y = 0.23(2\pi/a)$ in Fig. 3A. More remarkably, when one measures the relative spatial phase of these \vec{Q}_y dFF DW modulations at all stable vortex cores in Fig. 3B, the standard deviation is $\sim 12\%(2\pi)$ as shown in Fig. 3C. This can be seen directly by comparing the maxima of field-induced \vec{Q}_y dFF DW modulations (yellow) with the fine lines of constant reference phase for modulations at \vec{Q}_y , as shown in Fig. 3B. For clarity, the inset to Fig 3C shows a single example of how the phase of one dFF DW induced at a vortex can be compared to a

reference phase (grey lines). Overall, these data mean that the spatial phase of the field-induced nematic dFF DW within vortex cores is globally quite coherent. This is striking given how short-range, strongly phase-disordered and randomly oriented the DW is at zero field (17,32,42,43,46), but a theoretical mechanism does exist to lock the spatial phase when discrete symmetry breaking to nematic and commensurate density wave orders is caused by the field (26).

11 Finally, to search for $|\vec{k}(E)\rangle$ eigenstates at which mixing between of SC and DW components occurs, we first compare in Fig. 4A a typical conductance spectrum (44,45) at zero field (solid curve), with that at the center of a vortex placed at the same location by applying $B=8.5\text{T}$ (dashed curve). The primary differences are the suppression of the SC coherence peaks and the emergence of low-energy Bogoliubov quasiparticle states at the core (44,45). Next we measure $\langle \tilde{D}^{\delta Z}(\vec{Q}, |E|) \rangle$ and $\langle \tilde{S}^{\delta Z}(\vec{Q}, |E|) \rangle$ spatially averaged over all the vortex core regions (yellow Fig. 2F) and plot the results in Fig. 4B. The low-energy field-induced structure consisting of Bogoliubov core-states (44) exhibit s'-symmetry (red curve) that disappear quickly with increasing $|E|$. By contrast, we find the high energy field-induced modulations (Fig. 2C,D) exhibit a predominantly *d*-symmetry form factor with a maximum intensity near 28meV (blue curve). Thus, most of the dFF DW spectral weight is concentrated in the blue shaded vertical band of energies. The characteristic wavevectors $|\vec{k}(E)\rangle$ of states forming the field-induced dFF-DW at these energies are shown in Fig. 4D as blue circles; these are derived from analysis of the maxima at \vec{Q}_x and \vec{Q}_y of the dFF DW signature $\tilde{D}^{\delta Z}(\vec{q}, |E|)$ in Fig. 2D. To identify the Bogoliubov states $|\vec{k}(E)\rangle$ of the SC phase that are converted to these DW states by magnetic field, we next plot in Fig. 4C the measured angle β_k about the (π, π) point for each SC energy gap magnitude Δ_{SC} in zero field (Ref. 40,41). The \vec{k} -space locations of these Bogoliubov states are $|\vec{k}(E = \Delta_{SC})\rangle$ as determined using Bogoliubov quasiparticle scattering interference (40,41) and shown as

red dots in Fig. 4D. Clearly the locus of the predominantly DW states at high fields (blue circles) encapsulates that of some of the predominantly Bogoliubov eigenstates that existed at these same energies at zero field (red dots). Thus we discover that the intense dFF DW appearing within a radius of $\sim 2.5\text{nm}$ of each cuprate vortex center is formed by transforming from manifestly SC to manifestly dFF DW characteristics, a very specific set of $|\vec{k}(E)\rangle$ eigenstates whose locus is indicated by black circles in Fig. 4D. Such interconversion phenomena are as expected in general when PG intertwined/composite order exists, and are predicted for these specific $|\vec{k}(E)\rangle$ eigenstates in several such theories for cuprates.

11 Reiterating: by introducing sublattice phase-resolved imaging as a function of magnetic field, we find that a robust dFF DW is induced at each $\text{Bi}_2\text{Sr}_2\text{CaCu}_2\text{O}_{8+x}$ vortex core (Figs. 2C,E); that the induced dFF DW is nematic in the sense that it has predominantly the same unidirectional orientation for all cores (Fig. 3C); and that strong spatial phase coherence exists between these dFF DW regions (Fig. 3C,D). These data demonstrate directly that the field-induced interplay between the cuprate SC and dFF DW states occurs at the vortex cores. It is then plausible that, at highest magnetic fields, the coherent nematic dFF DW regions induced at each vortex will coalesce into a globally coherent smectic state with the same broken symmetries. Indeed, increasing coherence of the DW with increasing field has already been reported by NMR and X-ray studies (32,33). Intriguingly, the spatial-phase coherence of the isolated dFF DW regions (Fig. 3B,C) also implies that a mechanism exists to lock the phases (26), and thus that a microscopic coupling exists between the SC and dFF DW states. Finally, we discovered that the dFF DW induced at each core is generated by changing from SC to DW characteristics a small set of $|\vec{k}(E)\rangle$ eigenstates at eight specific \vec{k} -space locations (Fig. 4D). These are two key elements of the predicted phenomenology within models for the cuprate pseudogap where the superconductivity and the density wave are different facets of a single composite electronic order.

Figure Captions

Figure 1 d-Symmetry Form Factor Density Waves

- A. Schematic of phase diagram for the hole-doped CuO_2 plane. The region where PG, DW and SC phases are equivalent in strength, and thus most amenable to interconversion if a composite order exists, is indicated by the vertical arrow.
- B. One quarter of the CuO_2 Brillouin zone. Most theories for global PG order parameters that are a composite of a SC and DW components focus on the \vec{k} -space regions indicated by black circles (20,21,22,23,25,27).
- C. Measured $Z(\vec{r}, 100\text{meV})$ for underdoped $\text{Bi}_2\text{Sr}_2\text{CaCu}_2\text{O}_{8-x}$ showing the complex spatial arrangements of the disordered dFF-DW at zero field.
- D. From $Z(\vec{r}, 100\text{meV})$ in C we use sublattice phase-resolved visualization to determine $|\widetilde{D}^Z(\vec{q}, 100\text{meV})|$. The local maxima in $|\widetilde{D}^Z(\vec{q}, 100\text{meV})|$ at the two wavevector Q_x, Q_y as indicated by dashed red circles, are distinctive signatures of d -symmetry form factor modulations.
- E. Typical \vec{r} -space image of a cuprate d -symmetry form factor density wave; seeing this specific pattern in real space images is now the simplest way to detect a dFF-DW.

Figure 2 Signatures of dFF-DW Induced in $\text{Bi}_2\text{Sr}_2\text{CaCu}_2\text{O}_8$ - Vortex Cores

- A. The image here is $\delta g(\vec{r}, 10\text{meV})$ showing the field-induced low energy Bogoliubov quasiparticle patterns surrounding vortex cores; it is in excellent agreement with previous studies (44,45). While extremely important in that they provided first indication of the existence in r -space images of cuprate DW state, these Bogoliubov modulations at each vortex core cannot be the source of the DW existing at high fields outside the superconducting phase because (i) they have the wrong form factor (see below) and (ii) they must disappear when the superconductivity does.

- B. Sublattice phase-resolved $|\tilde{D}^{\delta Z}(\vec{q}, 10meV)|$ calculated from $\delta Z(\vec{r}, 10meV)$. There is no indication of d -symmetry form factor modulations induced by field at these low energies.
- C. $\delta Z(\vec{r}, 30meV, 8.5T)$ also shows additional states appearing at each vortex core. But because here the predominant effects are intra-unit-cell (13,17), it is difficult to detect the precise phenomena by eye in such a large FOV
- D. Sublattice phase-resolved $|\tilde{D}^{\delta Z}(\vec{q}, 30meV)|$ calculated from C. Here we see the clear signature of d -symmetry form factor modulations at Q_x and Q_y as indicated by red dashed circles.
- E. By zooming in on a single vortex core we can see by eye in $Z(\vec{r}, 30meV, 8.5T)$ that the field-induced r -space DW patterns induced are quite consistent with the dFF-DW shown in Fig 1E.
- F. Measured magnitude of $|\tilde{D}^{\delta Z}(\vec{r}, 30meV)|$ revealing that the regions supporting the field-induced dFF-DW occur at the sites of quantized vortex cores.

Figure 3 Global Spatial Phase Coherence of Field-induced Nematic dFF-DW

- A. Measured $|\tilde{D}^{\delta Z}(|q|, 30meV)|$ along the y -axis (blue) and x -axis (yellow) . This shows that in Fig. 2C,F the field-induced dFF-DW modulations are actually predominantly oriented along the y -axis where they are at least 3 times stronger than along x -axis.
- B. Measured amplitude and phase of the predominant Q_y dFF-DW states in all stable vortex cores of Fig 2C,E. To arrive at the blue/yellow representation of dFF DW modulation at each core, we take $\phi_y(\vec{r}) = \tan^{-1}[\text{Im}D_y(\vec{r})/\text{Re}D_y(\vec{r})]$ and then plot $\cos(\phi_y(\vec{r}))$ masked with radius 2nm (red dashed circle) around each stable vortex. The set of parallel grey lines shows a perfectly periodic modulation at wavelength $\lambda_y = 2\pi/Q_y$ that is used as a (arbitrary) reference phase. It can be seen by direct observation that the measured phase of Q_y dFF-DW states in all stable vortex cores is reasonably constant relative to the reference phase.

- C. Measured relative phase between Q_y dFF-DW states induced by field and the reference phase as shown in B. The measured relative phase variations are concentrated around a single value with a standard deviation of $\sim 12\%(2\pi)$; if the spatial phase of each Q_y dFF-DW modulation at a core were independent of all the others, this histogram would have \sim equal values in every bin. Inset shows direct comparison between measured spatial phase of a nematic dFF DW at one core and the reference phase. Thus the field-induced nematic dFF DW regions are strikingly spatially phase coherent while nevertheless remote from each other and with a robust SC state in between.

Figure 4 Interconversion between dSC and dFF-DW States at Vortex Cores

- A. Measured differential conductance spectrum at zero (solid) and high field (dashed) at the same location where a vortex is generated by applying a magnetic field. In the latter, the dSC coherence peaks are suppressed and low-energy Bogoliubov quasiparticle states emerge within the cores (44,45).
- B. Measured $|\tilde{D}^{\delta z}(\vec{Q}, |E|)|$ and $|\tilde{S}^{\delta z}(\vec{Q}, |E|)|$ averaged over all the vortex core regions (yellow in 2E). By correspondence with the spectra above in A, we see that low-energy Bogoliubov core-states actually have s' -symmetry (red) but this disappears quickly with increasing $|E|$. On the other hand, the high energy modulations have predominantly d -symmetry form factor with a maximum intensity near $|E|=28\text{meV}$ (vertical blue band).
- C. The angle β measured about the (π, π) for each measured SC energy gap Δ_{SC} at $B=0$ (40). These Bogoliubov quasiparticle interference data (red dots) are determined for measurements in the same FOV as in Figs. 2A,C; the relevant \vec{k} -space eigenstates can be identified from the known $|\vec{k}(E = \Delta_{SC})\rangle$ (40,41). The vertical blue shaded band indicates the energy at which the peak in dFF-DW amplitude occurs in Fig 4B. It contains only two points (red) where Bogoliubons exist at zero field (40,41).
- D. A diagram comparing states observed within the first Brillouin zone using QPI (40,41) and dFF DW (13,17) imaging techniques. Red dots show measured \vec{k} -space locus of

Bogoliubov quasiparticles (excitations of d -wave Cooper pairs) at $B=0$. Blue circles show the regions of \vec{k} -space generating the dFF DW states detected surrounding vortices at high B , in the same FOV. Our data (Fig. 4B,C) shows that eigenstates at $|E|=28\pm 5$ meV are interconverted by field from dSC Bogoliubov quasiparticles at \vec{k}_{SC} (red dots) to dFF-DW states at \vec{k}_{DW} (blue circles) . Therefore the interconversion process occurs manifestly at the eight momentum space regions indicated by black open circles. The diagonal dashed grey lines identify the antiferromagnetic Brillouin zone while the vertical/horizontal dashed grey lines are at $(0,3/4)\pi; (3/4,0)\pi$.

References

- 1 T. Timusk & B. Statt *Rep. Prog. Phys.* **62**, 61 (1999)
- 2 M. R. Norman, D. Pines, and C. Kallin *Adv. Phys.* **54**, 715-733 (2005)
- 3 D. Chowdhury and S. Sachdev, *Proceedings of the 50th Karpacz Winter School of Theoretical Physics* ; Preprint available at *arXiv:1501.00002* (2015).
- 4 S. Sachdev & R. La Placa, *Phys. Rev. Lett.* **111**, 027202 (2013)
- 5 M. R. Norman *Phys. Rev. B* **87**, 180506 (2013)
- 6 A. Allais, J. Bauer & S. Sachdev, *Phys. Rev. B* **90**, 155114 (2014).
- 7 M. H. Fischer *et al*, *New J. Phys.* **1**, 093057 (2014).
- 8 C. Chowdhury and S. Sachdev, *Phys. Rev. B* **90**, 245136 (2014)
- 9 W. A. Atkinson, A. Kampf, and S. Bulut, *New J. Phys.* **17**, 13025 (2015)
- 10 Y. Yamakawa & H. Kontani, *Phys. Rev. Lett.* **114**, 257001 (2015)
- 11 Long Zhang, Jia-Wei Mei, Preprint available *arXiv:1408.6592* (2015)
- 12 Wei-Lin Tu, Ting-Kuo Lee, Preprint available at *arXiv:1505.07728* (2015)
- 13 K. Fujita *et al*, *Proc. Nat'l. Acad. Sci.* **111**, E3026 (2014)
- 14 R. Comin *et al*, *Nature Materials* **6**, 1 (2015)
- 15 E. M. Forgan *et al*, Preprint at *arXiv:1504.01585* (2015)
- 16 Yang He, Ph.D. Thesis, Harvard University (2015)
- 17 M. Hamidian *et al* , Preprint available *arxiv.org/1507.07865* (2015)
- 18 E. Berg *et al*, *New J. Phys* **11**, 115004 (2009)
- 19 E. Fradkin, S. A. Kivelson, and J. M. Tranquada *Rev. Mod. Phys.* **87**, 457 (2015)
- 20 M.A. Metlitski and S. Sachdev, *New J. Phys.* **12** 105007 (2010)
- 21 K. B. Efetov, H. Meier & C. Pépin, *Nat. Phys.* **9**, 442 (2013)

-
- 22 H. Meier *et al*, *Phys. Rev. B* **88**, 020506(R) (2013)
- 23 C. Pépin *et al*, *Phys. Rev. B* **90**, 195207 (2014)
- 24 P. A. Lee *Phys Rev X* **4**, 31017 (2014)
- 25 Y. Wang, D. F. Agterberg, and A. Chubukov *Phys. Rev. Lett.* **114**, 197001 (2015)
- 26 S. A. Kivelson *et al*, *Phys. Rev. B* **66**, 144516 (2002)
- 27 Jay D. Sau and S. Sachdev, *Phys. Rev. B* **89**, 075129 (2014)
- 28 M. Einenkel *et al*, *Phys. Rev. B* **90**, 054511 (2014)
- 29 D.F. Agterberg and J. Garaud, *Phys. Rev. B* **91**, 104512 (2015)
- 30 S. E. Sebastian and C. Proust, *Annu. Rev. Condens. Matter Phys.* **6**, 411 (2015).
- 31 T. Wu *et al*, *Nature* **477**, 191 (2011)
- 32 J. Chang *et al. Nat. Phys.* **8**, 871 (2012)
- 33 T. Wu *et al. Nat Comm.* **4**, 1 (2013)
- 34 D. LaBoeuf *et al. Nat. Phys.* **9**, 79 (2013)
- 35 S. Blanco Canosa *et al. Phys. Rev. Lett.* **110**, 187001 (2013)
- 36 T. Wu *et al. Nat. Comm.* **6**, 1 (2015)
- 37 A.M. Mounce *et al. Phys. Rev. Lett* **106**, 057003 (2011)
- 38 S. Gerber *et al.* Preprint available at arXiv:1506.07910
- 39 A. J. Millis and M. R. Norman, *Phys. Rev. B* **76**, 220503(R) (2007).
- 40 K. Fujita *et al. Ch. 3, Strongly Correlated Systems - Experimental Techniques.* Springer (2014).
- 41 K. Fujita *et al, Science* **344**, 612 (2014)
- 42 S. Blanco-Canosa *et al. Phys Rev B* **90**, 054513 (2014)
- 43 M. Hücker *et al. Phys Rev B* **90**, 054514 (2014)

-
- 44 J.E. Hoffman, *et al. Science* **295**, 466 (2002).
45 T. Hanaguri *et al. Science* **323**, 923 (2009).
46 A. Mesaros *et al. Science* **333**, 426 (2011).

Acknowledgements: We are grateful to D. Agterberg, D. Chowdhury, A. Chubukov, R. Comin, A. Damascelli, E. Fradkin, D. Hawthorn, T. Hanaguri, S. Hayden, M.-H. Julien, S. A. Kivelson, M. Norman, and C. Pépin for very helpful discussions and communications. Experimental studies were supported by the Center for Emergent Superconductivity, an Energy Frontier Research Center, headquartered at Brookhaven National Laboratory and funded by the U.S. Department of Energy under DE-2009-BNL-PM015, as well as by a Grant-in-Aid for Scientific Research from the Ministry of Science and Education (Japan) and the Global Centers of Excellence Program for Japan Society for the Promotion of Science. S.D.E., J.C.D. and A.P.M acknowledge the support of EPSRC through the Programme Grant ‘*Topological Protection and Non-Equilibrium States in Correlated Electron Systems*’. Theoretical studies at Cornell University were supported by NSF Grant DMR-0955822. Theoretical studies at Harvard University were supported by NSF Grant DMR-1103860 and by the Templeton Foundation. Research at Perimeter Institute is supported by the Government of Canada through Industry Canada and by the Province of Ontario through the Ministry of Research and Innovation.

FIG 1

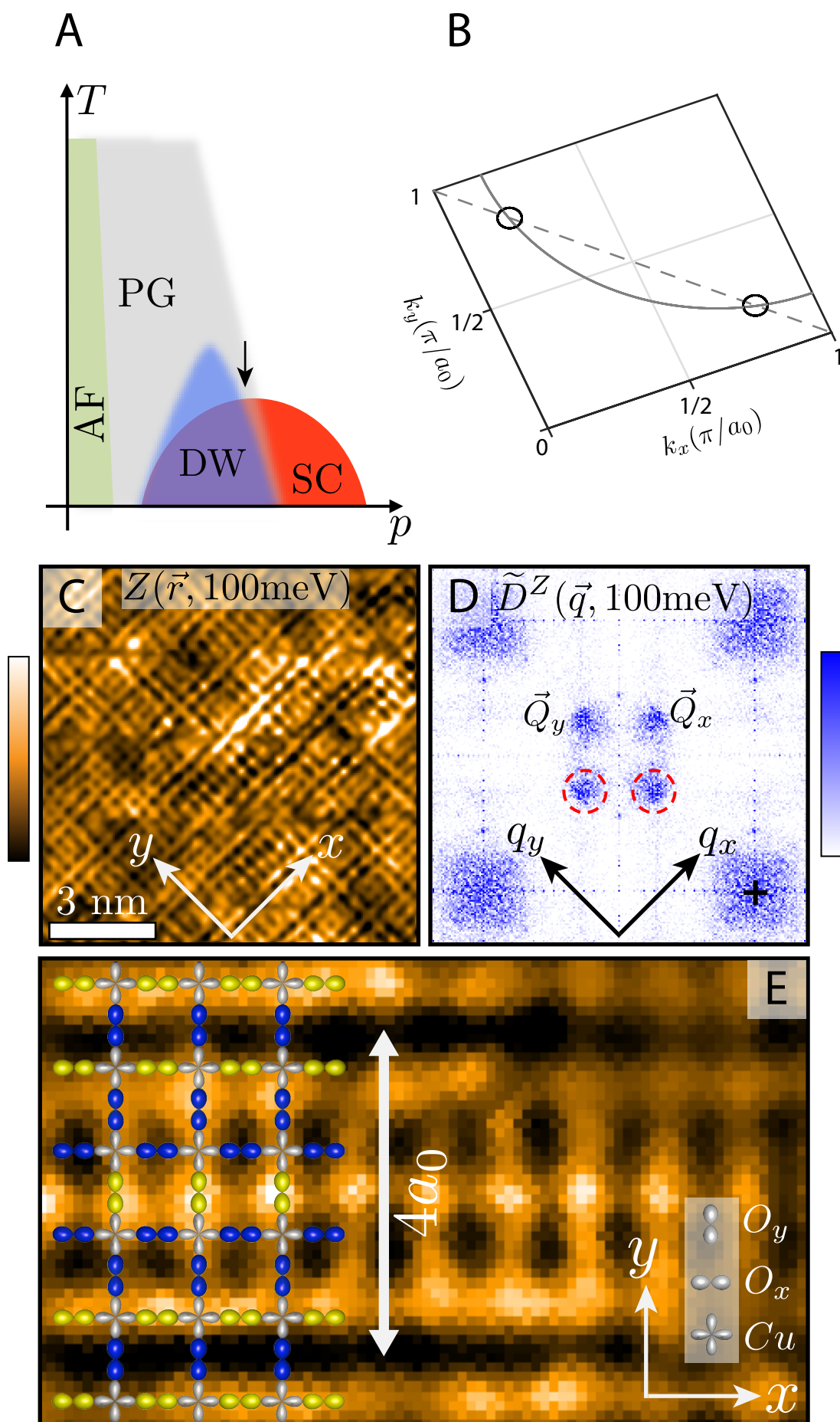


FIG 2

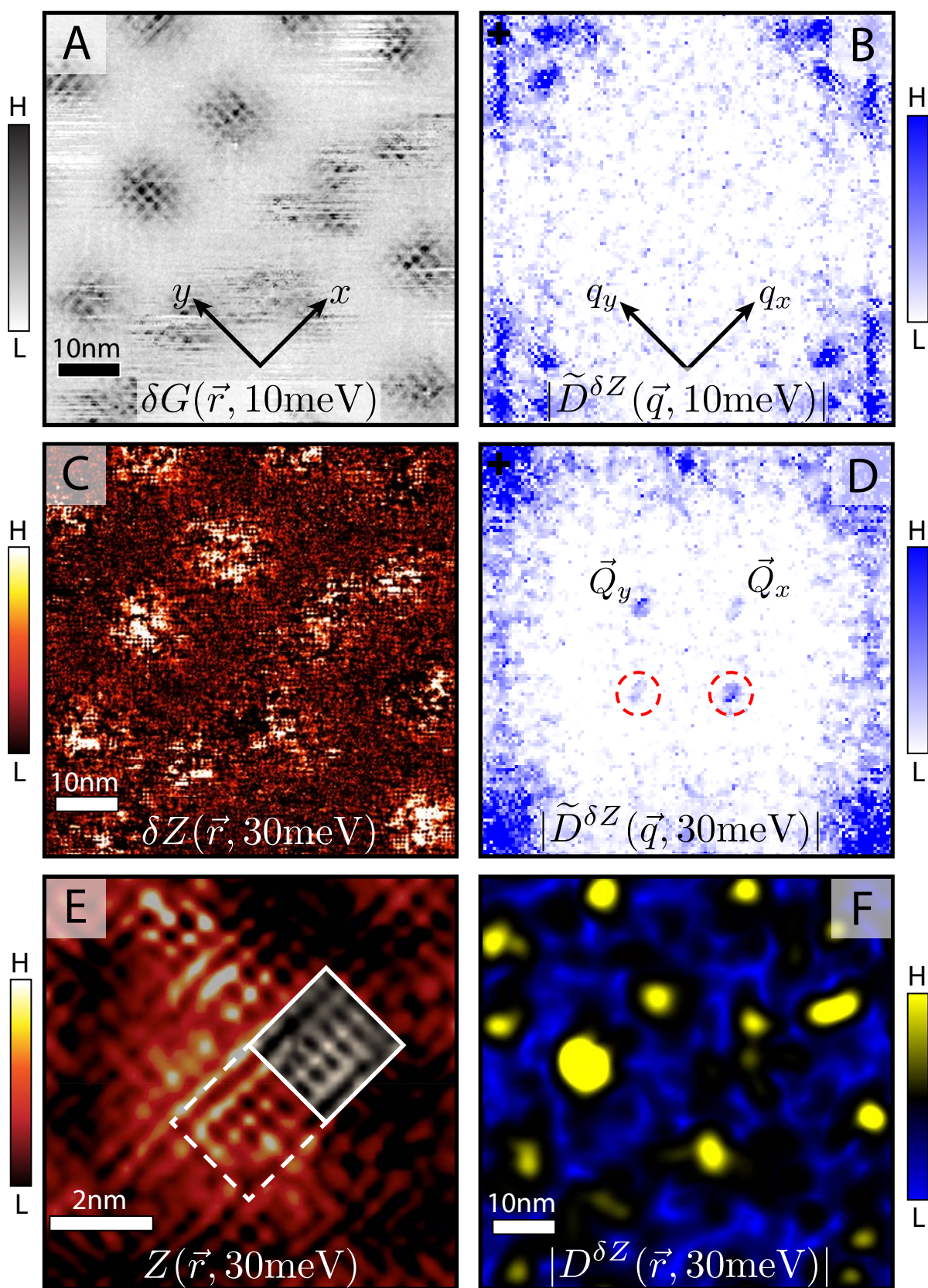


FIG 3

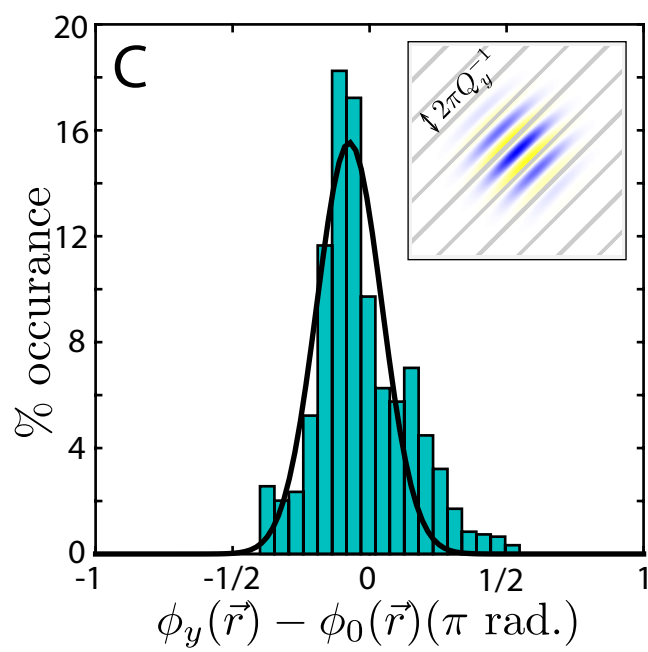
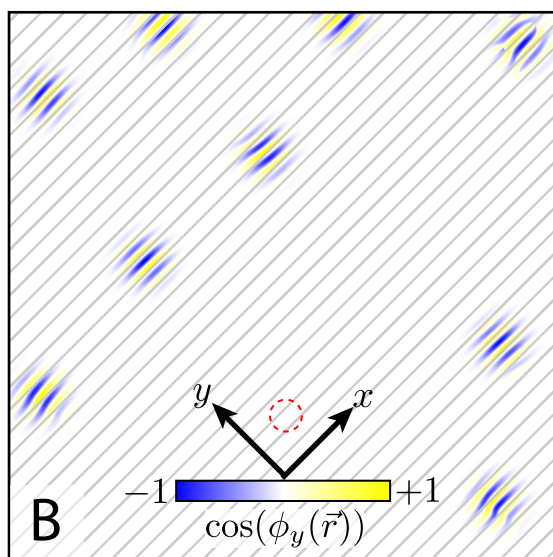
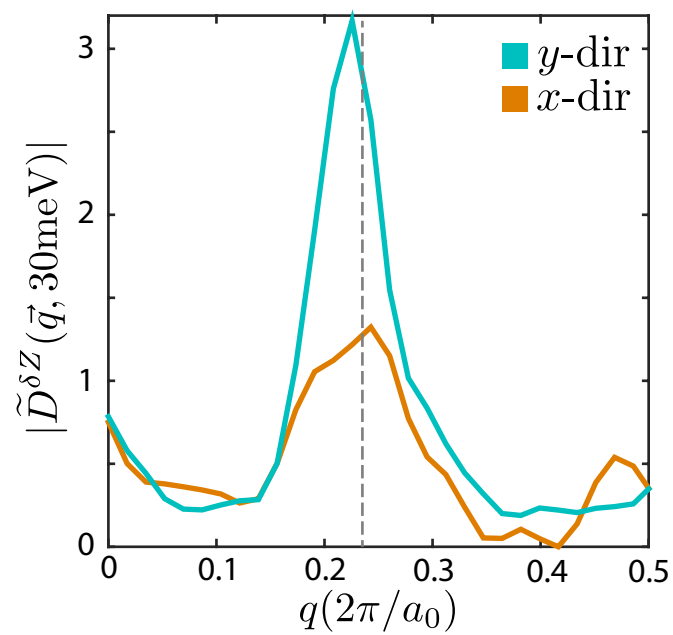
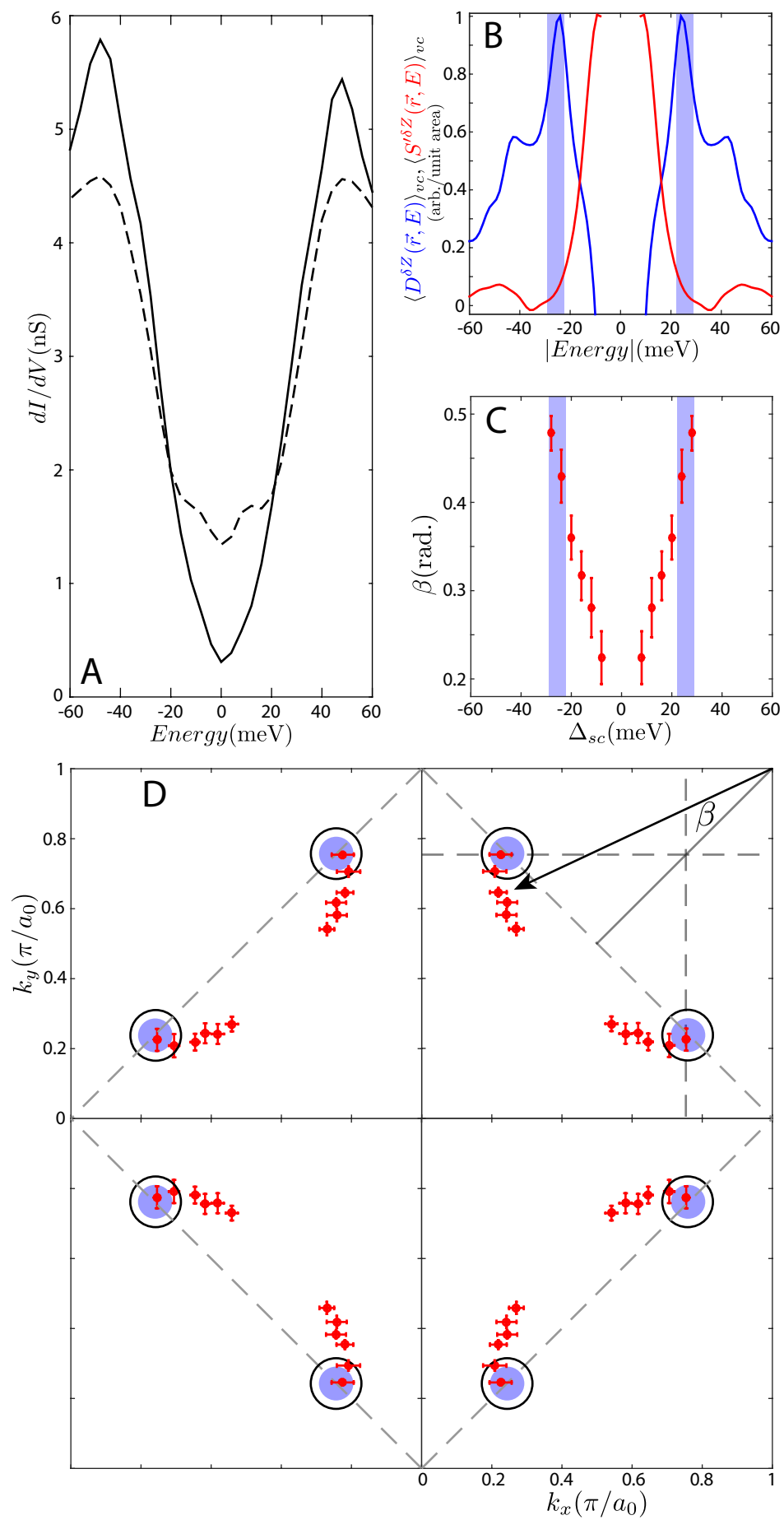


FIG 4



Supplementary Materials for

Magnetic-field Induced Interconversion of Cooper Pairs and Density Wave States within Cuprate Composite Order

M. H. Hamidian, S.D. Edkins, K. Fujita, A. Kostin, A. P. Mackenzie,
H. Eisaki, S. Uchida, M. J. Lawler, E.-A. Kim, S. Sachdev, and J. C. Davis*

*To whom correspondence should be addressed - Email : jcseamusdavis@gmail.com

Materials and Methods

For our studies, high-quality $\text{Bi}_2\text{SrCaCu}_2\text{O}_{8+\delta}$ single crystals were grown using the travelling-solvent-floating zone (TSFZ) method. The samples are of $\text{Bi}_{2.1}\text{Sr}_{1.9}\text{CaCu}_2\text{O}_{8+\delta}$ and were synthesized from dried powders of Bi_2O_3 , SrCO_3 , CaCO_3 and CuO . The crystal growth was carried out in air and at growth speeds of 0.15-0.2 mm/h for all samples. Inductively coupled plasma (ICP) spectroscopy was used for the composition analysis and a vibrating sample magnetometer (VSM) was used for measurement of T_c .

Here we studied samples of $\text{Bi}_2\text{SrCaCu}_2\text{O}_{8+\delta}$ with hole doping $p \cong 0.17$. Each sample was inserted into the cryogenic ultra high vacuum of the SI-STM system and cleaved to reveal an atomically flat BiO surface. All measurements were performed at a temperature of 2K. The basic spectroscopic imaging STM consists of lock-in amplifier measurements of the differential tunneling conductance with atomic resolution and register, as a function of both location \vec{r} and electron energy E . We vary the applied magnetic field perpendicular to the CuO_2 planes of the samples using a superconducting solenoid with a highly stable persistent current/field.

Supporting Text and Figures

(I) Form Factor of CuO₂ IUC States

Here we present a mathematical description of the form factor organization of density waves on the CuO₂ plane. The different density waves form factors are due to periodic modulation of the $\vec{Q} = 0$ form factors, whose point group symmetry is well defined. Modulating these form factors with wave-vector $\vec{Q} \neq 0$, one obtains

$$A_S(\vec{r}) = \begin{cases} S \cos(\vec{Q} \cdot \vec{r} + \phi_S), & \vec{r} = \vec{r}_{Cu}, \\ 0, & \vec{r} = \vec{r}_{O_x}, \\ 0, & \vec{r} = \vec{r}_{O_y}, \end{cases} \quad A_{S'} = \begin{cases} 0, & \vec{r} = \vec{r}_{Cu}, \\ S' \cos(\vec{Q} \cdot \vec{r} + \phi_{S'}), & \vec{r} = \vec{r}_{O_x}, \\ S' \cos(\vec{Q} \cdot \vec{r} + \phi_{S'}), & \vec{r} = \vec{r}_{O_y}, \end{cases}$$

$$A_D(\vec{r}) = \begin{cases} 0, & \vec{r} = \vec{r}_{Cu}, \\ D \cos(\vec{Q} \cdot \vec{r} + \phi_D), & \vec{r} = \vec{r}_{O_x}, \\ -D \cos(\vec{Q} \cdot \vec{r} + \phi_D), & \vec{r} = \vec{r}_{O_y}, \end{cases} \quad (S1.1)$$

In the CuO₂ plane of cuprates, \vec{r}_{Cu} , \vec{r}_{O_x} and \vec{r}_{O_y} are the Cu, O_x and O_y sublattice sites, and $\phi_{S,S',D}$ are the phases of each of the density wave form factor components. Equation S1.1 shows that a purely *d*-symmetry form factor density wave can be thought of as a wave on each of the oxygen sub-lattices but with a spatial phase shift of π between them.

The consequences of a primarily *d*-symmetry form factor density wave for the two key functions used to measure modulations with *S'* and *D* form factor symmetry in the main text,

$$\tilde{S}'(\vec{q}) = (\tilde{O}_x(\vec{q}) + \tilde{O}_y(\vec{q}))/2 \quad (S1.2)$$

$$\tilde{D}(\vec{q}) = (\tilde{O}_x(\vec{q}) - \tilde{O}_y(\vec{q}))/2 \quad (S1.3)$$

, are discussed below.

A purely d -symmetry form factor density wave has modulations in anti-phase on the x and y oxygen sub-lattices (Fig. S1A). For the specific example of $\vec{Q}_x \approx (\frac{1}{4}, 0)$, $\vec{Q}_y \approx (0, \frac{1}{4})$ considered in our study, this requires that the peaks at $\pm\vec{Q}_x$ and $\pm\vec{Q}_y$ present in both $\tilde{O}_x(\vec{q})$ and $\tilde{O}_y(\vec{q})$ must cancel exactly in $\tilde{S}'(\vec{q}) = (\tilde{O}_x(\vec{q}) + \tilde{O}_y(\vec{q}))/2$ and be enhanced in $\tilde{D}(\vec{q}) = (\tilde{O}_x(\vec{q}) - \tilde{O}_y(\vec{q}))/2$. Conversely the peaks at $\vec{Q}' = (1,0) \pm \vec{Q}_{x,y}$ and $\vec{Q}'' = (0,1) \pm \vec{Q}_{x,y}$ will be enhanced in $\tilde{S}'(\vec{q})$ but will cancel exactly in $\tilde{D}(\vec{q})$ (Figs S1B,C).

This occurs because the two sub-lattices have modulations at the same wave-vector but with a π phase shift between them. Importantly, electronic structure images formed using the difference of oxygen sub-lattices, as in $\tilde{D}(\vec{q})$, have the effect of removing this phase difference and recovering the peaks in the Fourier transform at the fundamental wave-vectors. These are necessary consequences of a density wave with a primarily d -symmetry form factor and hold for any d -symmetry form factor modulation in the presence of arbitrary amplitude and overall phase disorder.

(II) Sub-Unit-Cell Resolution Field Dependent Imaging

To demonstrate the high precision of spatial registration between the data sets taken at $B = 0T$ and $B = 8.5T$, we show in figure S2 the processed topographic images acquired simultaneously with the spectroscopic maps. These data sets, which are analyzed and presented in the main text, were taken 2 weeks apart in the same region of the sample. The raw data for all data sets were phase corrected using the

Lawler-Fujita distortion-correction algorithm (see ref. 1), mapping the data onto a perfectly periodic lattice free of lattice distortions due to systematic measurement effects. A morphing scheme was then implemented to register all data sets in the same field of view (FOV) to one another with ~ 10 picometer precision. This method allows meaningful subtraction of high and low field data to detect magnetic field induced differences of the electronic structure at the sub-unit-cell scale.

(III) Spatial Mapping of Form Factor Amplitudes

Determination of the local amplitude of density wave modulations in the S' and D symmetry form factor projections may be achieved through Fourier filtration of the measured functions

$$\tilde{D}^{\delta Z}(\vec{q}, |E|) = \tilde{O}_x(\vec{q}, V) - \tilde{O}_y(\vec{q}, V) \quad (\text{S3.1})$$

$$\tilde{S}'^{\delta Z}(\vec{q}, |E|) = \tilde{O}_x(\vec{q}, V) + \tilde{O}_y(\vec{q}, V) \quad (\text{S3.2})$$

to select the amplitude contained in the region of reciprocal space proximately surrounding \vec{Q}_x and \vec{Q}_y . The function $\tilde{D}^Z(\vec{q}, |E|)$ is multiplied by a gaussian of FWHM $2\sqrt{2\ln 2}\Lambda$ centred on \vec{Q}_x and \vec{Q}_y respectively to create two filtered complex Fourier transforms $\tilde{D}_x^{\delta Z}(\vec{q}, |E|)$ and $\tilde{D}_y^{\delta Z}(\vec{q}, |E|)$.

$$\tilde{D}_{x,y}^{\delta Z}(\vec{q}, |E|) = 2\tilde{D}^{\delta Z}(\vec{q}, |E|)e^{-\frac{(\vec{q}-\vec{Q}_{x,y})^2}{2\Lambda^2}} \quad (\text{S3.3})$$

Here, the factor of two arises from the fact that we have only filtered around $\vec{Q}_{x,y}$ and not $-\vec{Q}_{x,y}$ which, by the inversion symmetry of the Fourier transform of real functions, contain identical information. By taking the modulus of their inverse Fourier transforms one obtains an estimate of the amplitude of the x and y directed modulations.

$$|\tilde{D}_{x,y}^{\delta Z}(\vec{r}, |E|)| = \left| \frac{1}{(2\pi)^2} \int d\vec{q} e^{i\vec{q}\cdot\vec{r}} \tilde{D}_{x,y}(\vec{q}) \right| \quad (\text{S3.4})$$

The summed amplitude in the d-Symmetry form factor projection at wave-vectors \vec{Q}_x and \vec{Q}_y is then given by

$$|\tilde{D}^{\delta Z}(\vec{r}, |E|)| = |\tilde{D}_x^{\delta Z}(\vec{r}, |E|)| + |\tilde{D}_y^{\delta Z}(\vec{r}, |E|)| \quad (\text{S3.5})$$

. The same procedure may be applied to $\tilde{S}^{\delta Z}(\vec{q}, |E|)$ to obtain $\tilde{S}'^{\delta Z}(\vec{r}, |E|)$.

(III) Spatial Phase Coherence of Induced Density Wave at Vortices

Figure 3 of the main text presents analysis demonstrating that there is a high level of spatial phase coherence between the dFF-DW modulations found in vortex regions. The analysis method proceeds as follows:

- 1) Using the sublattice segregation method described in the main text, generate the complex function $\tilde{D}^{\delta Z}(\vec{q}, E)$, which measures the spectral weight of the field induced dFF-DW.
- 2) Individually filter $\tilde{D}^{\delta Z}(\vec{q}, E)$ around the points \vec{Q}_x and \vec{Q}_y with a filter of width Λ to obtain $\tilde{D}_{x,y}(\vec{q}, E) = 2\tilde{D}^{\delta Z}(\vec{q}, E)e^{-\frac{(\vec{q}-\vec{Q}_{x,y})^2}{2\Lambda^2}}$
- 3) Inverse Fourier transform to obtain $D_{x,y}(\vec{r}) = \text{Re}D_{x,y}(\vec{r}) + i\text{Im}D_{x,y}(\vec{r}) = \frac{1}{(2\pi)^2} \int d\vec{q} e^{i\vec{q}\cdot\vec{r}} \tilde{D}_{x,y}(\vec{q})$. This function contains the real space structure of dFF-DW modulation along each of the two directions, including spatially dependent phase and amplitude information.
- 4) Generate a spatial phase map for modulations along \vec{Q}_x and \vec{Q}_y : $\phi_{x,y}(\vec{r}) = \tan^{-1}[\text{Im}D_{x,y}(\vec{r}) / \text{Re}D_{x,y}(\vec{r})]$.
- 5) To arrive at the blue and yellow images of Fig. 3B, we take $\cos(\phi_y(\vec{r}))$ and mask around the vortex regions. The resulting image shows the dFF-DW modulations at just the vortex sites.
- 6) To determine phase coherence we construct a reference modulation $\cos(\phi_{ref}(\vec{r}))$ where $\phi_{ref}(\vec{r}) = \vec{Q}_y \cdot \vec{r} + \phi_0$. The thin grey lines in Fig. 3B represents the points at which the phase of the reference function is

$0 \bmod 2\pi$. More simply the represent the crests of a wave with same wavevector as the field-induced modulations Q_y .

- 7) Fig. 3C is then produced by taking the histogram of the quantity $\phi_y(\vec{r}) - \phi_{ref}(\vec{r})$ at only the vortex regions.

A common radius of 20\AA around each vortex region was used and not all vortices were included in the histogram as some were too unstable. In total, 6 of 9 vortices were used in the histogram.

References

1. M. J. Lawler *et al*, Nature **446** 347–351 (2010)

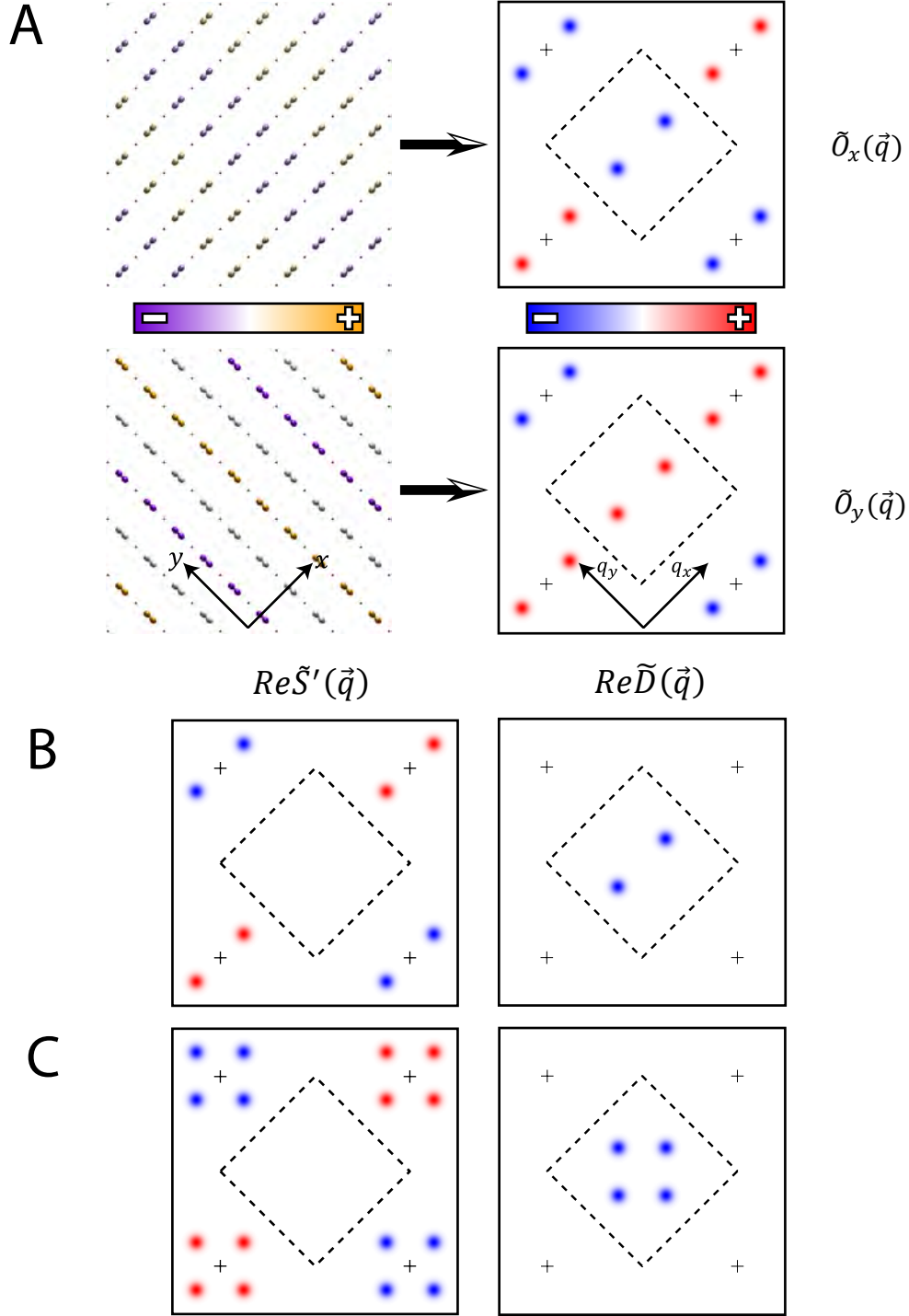


Figure S1: Fourier Analysis of the Density Wave (A) Schematic of the segregated sublattice images $O_{x,y}(\vec{r})$ and their Fourier transforms $\tilde{O}_{x,y}(\vec{q})$ (B) $Re\tilde{S}'(\vec{q})$ and $Re\tilde{D}(\vec{q})$ for a d form factor density wave with modulation along the x direction at $\vec{Q}=(Q,0)$. Note that the origin coordinates in real space as chosen such that the Fourier transforms are purely real. (C) $Re\tilde{S}'(\vec{q})$ and $Re\tilde{D}(\vec{q})$ for a d form factor density wave with modulations along the x and y directions at $\vec{Q}=(Q,0), (0,Q)$. The key signature of the d form factor is the absence of the peaks at $(Q,0), (0,Q)$ in $Re\tilde{S}'(\vec{q})$ and their presence in $Re\tilde{D}(\vec{q})$; the converse being true for the DW peaks surrounding $(\pm 1, 0)$ and $(0, \pm 1)$.

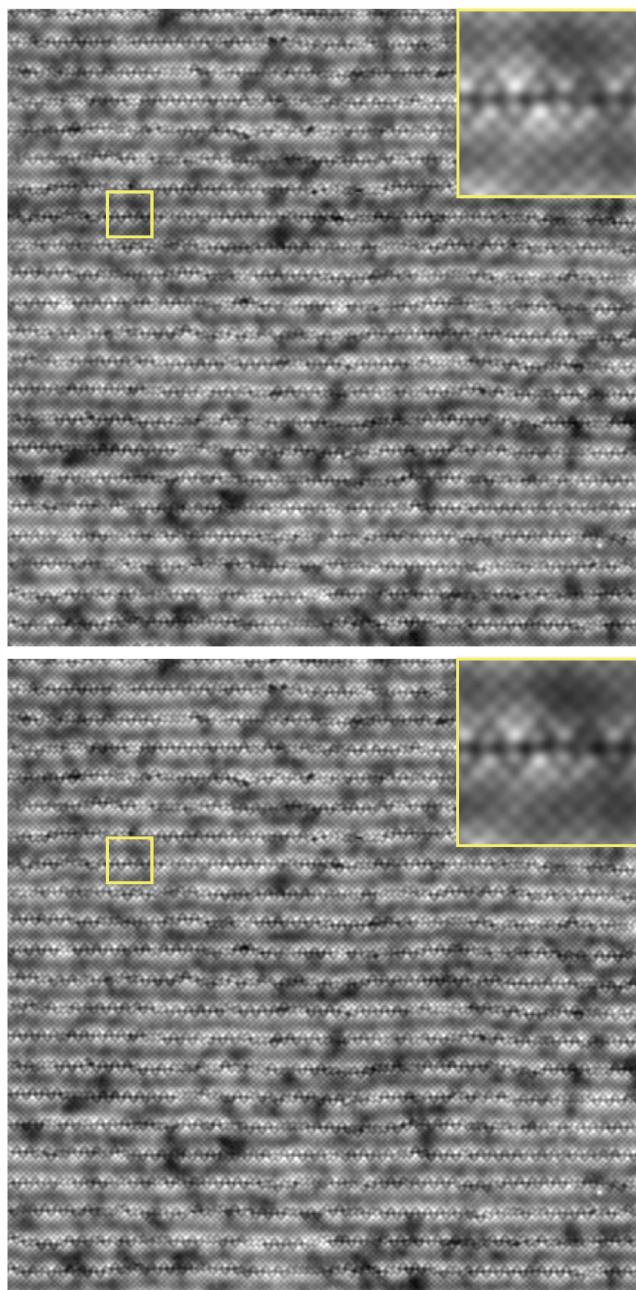


Figure S2: Spatially Registered B=8.5T and B=0T Topographs After LF-correction and morphing registration, the position of the atoms in the B=8.5T (upper panel) and B=0T data sets (lower panel) are registered to within 10pm. The images show a 65nmx65nm region of the sample.. Insets show magnified images of the region indicated by the yellow squares